The 9th International Supercritical CO_2 Power Cycles Symposium
March 2 – 5, 2026, Pittsburgh, PA
Paper 66

Development of Electric Machines that Produce Radial Magnetic Forces to Statically Unload Foil Bearings and Enable Hermetic sCO_2 Turbomachinery

Sayed Saleh
Graduate Researcher
University of Minnesota
Minneapolis, MN

Sayed Saleh is a PhD candidate, focusing on designing electric machines, creating torque and force to assist foil bearings in hermetically sealed turbomachinery.

Takahiro Noguchi
Postdoctoral Associate
University of Minnesota
Minneapolis, MN

Takahiro Noguchi is a postdoctoral associate, working on designing electric machines and developing control systems for bearingless motors.

Logan Rapp
Mechanical Engineer
Sandia National Lab.
Albuquerque, NM

Logan Rapp is a Mechanical Engineer at Sandia National Laboratories and leads supercritical carbon dioxide (sCO2) Brayton cycle development.

Eric Severson
Associate Professor
University of Minnesota
Minneapolis, MN

Eric Severson is an associate professor who specializes in electric machines research, including bearingless motors, magnetic bearings, and flywheel energy storage.

Abstract

This paper explores the development of electric machines that produce radial forces to assist foil bearings in hermetic supercritical carbon dioxide (sCO_2) turbomachinery. While there is growing interest in hermetic sCO_2 turbomachinery for power-cycle applications, the absence of a suitable oil-free bearing technology has emerged as a limiting factor for large-scale deployment. Foil bearings are a promising oil-free solution that are successfully used with small shafts, but experience significant wear at low rotational speeds when used with the heavy shafts inherent to energy applications. In prior work, the authors proposed designing electric machines capable of producing both torque and radial forces to offload foil bearings during low-speed operation. This paper extends the prior work by considering case study machines in the sCO_2 environment. This paper presents a practical implementation to realize these machines for hermetic sCO_2 turbomachinery, characterized by high pressure, elevated temperature, and high shaft speed. FEA models are developed to evaluate the electromagnetic performance of electric machines acting as foil-bearing unloaders and thermal resistance networks are used to model thermal aspects relevant to operation in an sCO_2 environment. The case study machines leverage sCO_2 leakage flow from the compressor side, drawn through the airgap using a scavenging pump, to maintain winding and permanent-magnet temperatures within safe limits. Overall, this paper outlines the practical implementation of electric machines assisting foil bearings in hermetic sCO_2 turbomachinery and illustrates their performance potential.

Keywords: Electric motors, sCO_2 power cycles, gas foil bearing, foil bearing unloader

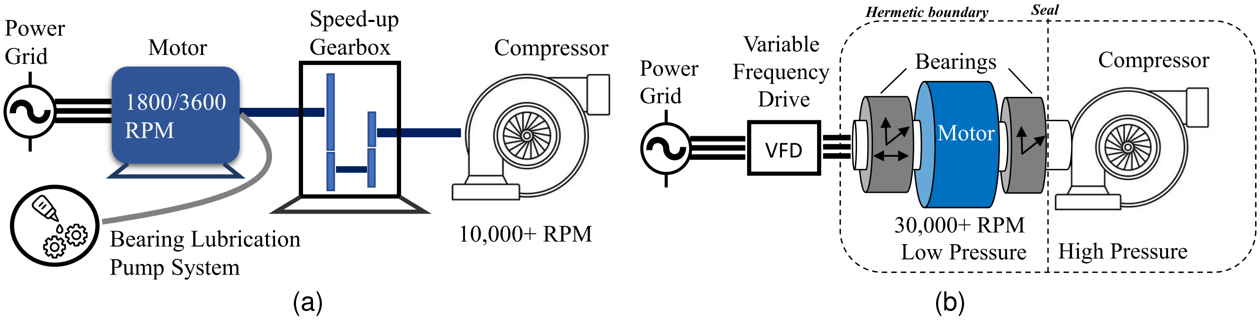

Fig. 1: Schematic of (a) the legacy turbomachinery system topology featuring a lubrication system and gearbox, (b) the modern direct-drive hermetically sealed turbomachinery system topology [3].

1 Introduction

Supercritical carbon dioxide (sCO_2) power cycles have gained renewed momentum with the development of experimental prototypes across various power scales worldwide [1]. Motivated by these developments, interest in closed Brayton cycles for power generation has expanded as researchers seek alternatives to conventional open Brayton and steam Rankine systems. A closed sCO_2 Brayton cycle attains higher thermal efficiency because near-critical CO_2 exhibits high density (enabling compact turbomachinery), reduced compression work, and strong recuperation effectiveness that raises overall cycle performance [2]. These attributes facilitate thermal integration with a diverse set of heat sources, including waste-heat recovery, advanced nuclear, concentrated solar power, and thermal energy storage. Beyond its thermodynamic advantages, this cycle eliminates water from the process, a benefit that is particularly valuable for mobile power units and installations operating in remote environments. To realize these advantages in practical systems, the turbomachinery must operate within a sealed environment capable of handling high pressures and preventing CO_2 leakage.

Figure 1 shows two turbomachinery configurations. The legacy arrangement (Fig. 1a) is the traditional industrial topology for pumps, compressors, and generators. Although robust and mature, this approach is maintenance-intensive, requires bulky components, and relies on dry-gas seals and gearboxes to match a low-speed electric motor to a high-speed compressor which create losses and reliability concerns. Due to these drawbacks, there is growing interest in instead utilizing fully hermetic designs in which a high-speed generator and bearings operate directly in the process fluid. Modern power electronics and high-speed drives enable compact, efficient, direct-drive machinery [3], as shown in Fig. 1b. By coupling the motor and compressor directly and employing variable-frequency drives (VFDs), the gearbox is eliminated, improving efficiency [4]. Moreover, the sealed architecture of hermetic turbomachines prevents external leakage and internal contamination [5]. Therefore, this configuration is especially attractive for sCO_2; however, hermetic turbomachines face two main challenges due to the process fluid conditions and hermetic constraints [6, 7].

The first challenge arises from the direct contact between the process fluid and the bearings, which creates integration difficulties in sCO_2 power cycles because the solvent properties of sCO_2 can dissolve the lubricants used in traditional bearings [8]. The second challenge stems from the sealed nature of hermetic turbomachinery, which restricts both electrical and mechanical passthroughs. Together, these issues narrow the choice of bearing type and necessitate the use of oil-free bearings [9]. To overcome these challenges, two promising bearing solutions are available: process-gas-lubricated bearings (foil or externally pressurized) and active magnetic bearings (AMBs). Among these, foil bearings (Fig. 2a) are the lowest-cost option, as they require no lubrication systems or additional passthroughs, making them the simplest to integrate into sealed environments [10]. However, foil-bearing applications have been limited to applications with lighter weight shafts (typically <200 kW power systems) because foil bearings make mechanical contact with the

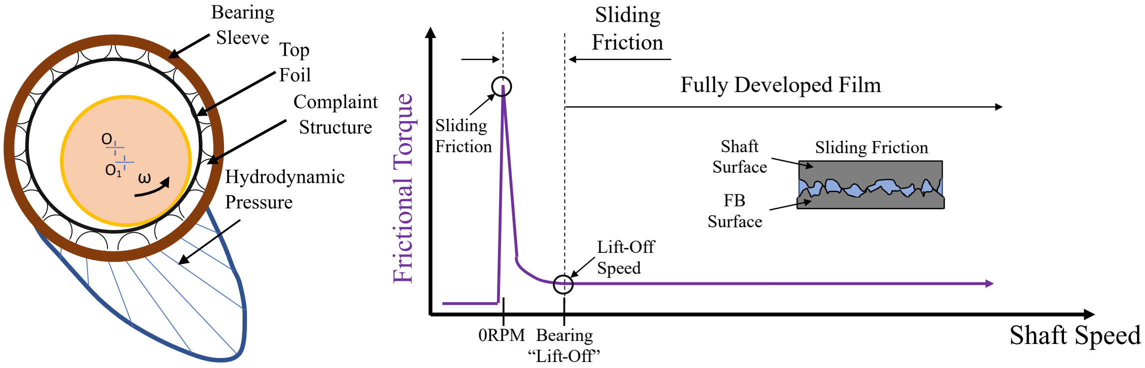

(a) (b)

Fig. 2: (a) Foil-bearing structural components, and (b) foil-bearing frictional torque versus shaft speed [7].

shaft journal at low speeds [7, 11]. To address this, the authors proposed developing electric machines that can produce radial magnetic forces to unload foil bearings during low-speed operation in [12]. This prior work focused on exploring the design space of these electric machines and showed that it is feasible to develop high-performance designs capable of unloading their shaft weight without compromising power density and efficiency. The present paper now selects optimal designs from the design space of the prior study and presents a detailed analysis of these designs' performance as both bearing unloaders and electric motor/generators within the sCO_2 environment.

The primary contribution of this paper is to investigate the implementation of electric machines that function as foil-bearing unloaders in sCO_2 turbomachinery by (i) introducing sCO_2 specific thermal considerations, and (ii) evaluating their force performance while functioning as unloaders. The paper is organized as follows. Section 2 explains the proposed foil-bearing unloader. Section 3 describes the strategy for evaluating the proposed unloader in an sCO_2 environment, with a focus on techniques used to keep the machine within thermal limits. Section 4 presents a combined thermal and FEA study of example foil bearing unloader designs.

2 Foil Bearing Unloader

This section explains the motivation for unloading of foil bearings and presents the proposed foil bearing unloader concept based around an electric machine that is capable of creating a constant radial force.

2.1 Foil Bearing Limitations

Figure 2b illustrates foil-bearing behavior during low-speed and normal operation. During low speeds (i.e., below the lift-off speed), the shaft is supported directly on the foil surfaces. As rotation begins, sliding contact and friction produce a characteristic startup torque spike. With increasing shaft speed, the bearing reaches full hydrodynamic lift-off (i.e., normal operation), where a stable gas film entirely separates the shaft from the foils. The lift-off/touchdown speed depends on the bearing dimensions and load, but is often estimated to be approximately 20% of the machine's rated speed [13]. Because foil bearings endure repeated start–stop cycles involving sliding contact, wear is inevitable. In practice, wear is exacerbated for heavier shafts, thereby shortening bearing lifetime and limiting foil bearings in hermetic turbomachinery to lightly loaded applications, with most deployments below 200 kW [6].

To address the inherent limitations of foil bearings at low speeds, the concept of a bearing unloader has been considered by multiple papers. Bearing unloaders create hybrid systems that combine the strengths of foil bearings with those of other technologies, such as magnetic or hydrostatic bearings. For example, Swan-

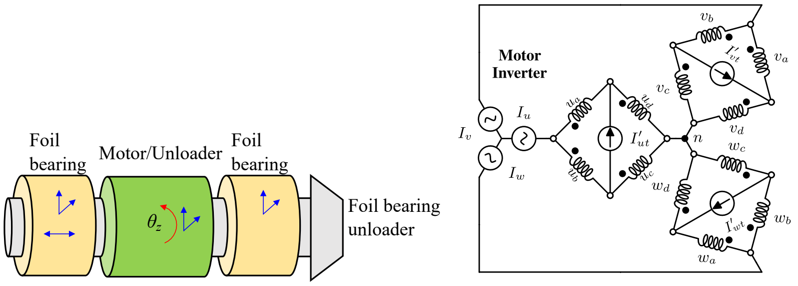

(a) (b)

Fig. 3: (a) Conceptual view of the proposed foil bearing unloader, and (b) bridge winding layout; the force producing drive is shown as current sources inside the Wheatstone bridge winding configuration.

son et al. [14] demonstrated a hybrid support system where an active magnetic bearing supports the rotor at low speeds, while foil bearings provide full support at high speeds. While these systems substantially reduce wear, the inherent drawbacks of AMBs remain, including complex control requirements, a large number of connections (passthroughs into the hermetic environment), and the need for additional shaft length, which can adversely affect high-speed performance.

In previous work [3], the authors reviewed several bearing-unloader concepts that can assist foil bearings and suggest leveraging “bearingless" motor technology [15] to create an electric machine capable of controlling a constant radial force to enable foil bearing implementation in large sCO_2 turbomachinery. The goal of these machines is to unload the shaft’s static weight to assist foil bearings only at low speeds, where they would otherwise experience wear. The next subsection explains this proposed unloader.

2.2 The Proposed Foil Bearing Unloader

Figure 3a shows a conceptual view of the proposed unloader. Here, the electric motor is designed to create a constant radial force to counteract static loads (i.e., shaft weight). To create both torque and radial forces using electric motors, the stator windings need to be designed to produce two independent magnetic fields [15, 16]: a torque-producing field with p pole-pairs and a suspension-force–producing field with $p_s = p \pm 1$ pole-pairs. There are two types of winding configurations to create these magnetic fields: (1) installing an additional winding with distinct coils dedicated separately to torque and suspension force (“separate windings”), or (2) designing a single stator winding that simultaneously produces both torque and suspension force (“combined windings”). Combined windings can be divided into several configurations, i.e., bridge, parallel, mid-point current injection (MCI), and multiphase (MP). The advantages and trade-offs of each topology are summarized in [17].

In recent work, the authors compared these winding configurations against the requirements of the proposed unloader [12] and found the bridge winding (Fig. 3b) particularly compelling for two reasons. First, it enables full independence between the torque and suspension drives, allowing conventional three-phase variable-speed drives to be used without awareness of the machine’s radial-force capability. Second, it enables full use of torque capacity when bearing unloading is not required. The same study explored the design space of the proposed unloader through multi-objective optimization and found that it is possible to unload the foil bearings at low speed while retaining high efficiency and high power density at high speeds when the unloading forces are not required. However, this prior study did not examine machine behavior in an sCO_2 environment. Building on that work, the following sections evaluate the unloader under realistic sCO_2 operating conditions, accounting for motor-cavity temperature, pressure, and cooling requirements.

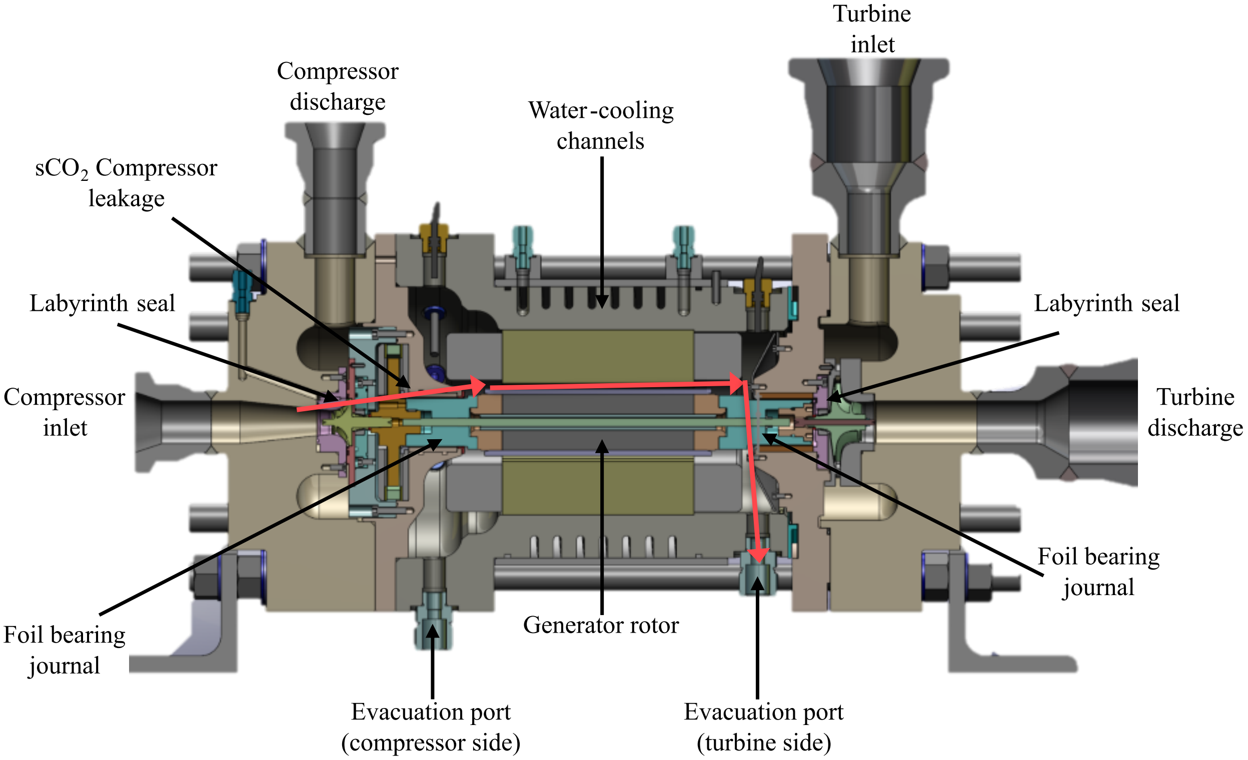

Fig. 4: Sandia National Laboratory sCO$_2$ turbogenerator demonstration machine showing the design with gas foil bearings, labyrinth seals, and a PM rotor for the turbine-alternator-compressor (TAC) design, along with the proposed leakage flow path for cooling the machine, as indicated by the red arrow.

3 Evaluation Strategy for Foil Bearing Unloader in sCO$_2$ Environment

This section explains the strategy used to evaluate the proposed unloader in sCO$_2$ environments by considering electric machine designs to replace an existing electric machine in a professionally designed hermetic turbomachine demonstrator [18]. This demonstrator, shown in Fig. 4, is supported by two radial foil bearings and uses a scavenging pump (Fig. 5a) to maintain a low-pressure generator cavity. The operating specifications are provided in Table 1. The section begins by describing the different heat sources within the motor cavity and the methods employed to estimate the machine losses. Then, two machines from the optimization study in [12, Sec. IV] are selected as case studies for further evaluation in an sCO$_2$ environment. Finally, practical thermal considerations are discussed to ensure that the motor components remain within their allowable temperature limits.

Table 1: Operating specifications for the demonstration machine.

Parameter	**Value**
Compressor outlet pressure	17 MPa
Cavity pressure	2 MPa
Compressor inlet temperature	32 °C
Turbine inlet temperature	536 °C

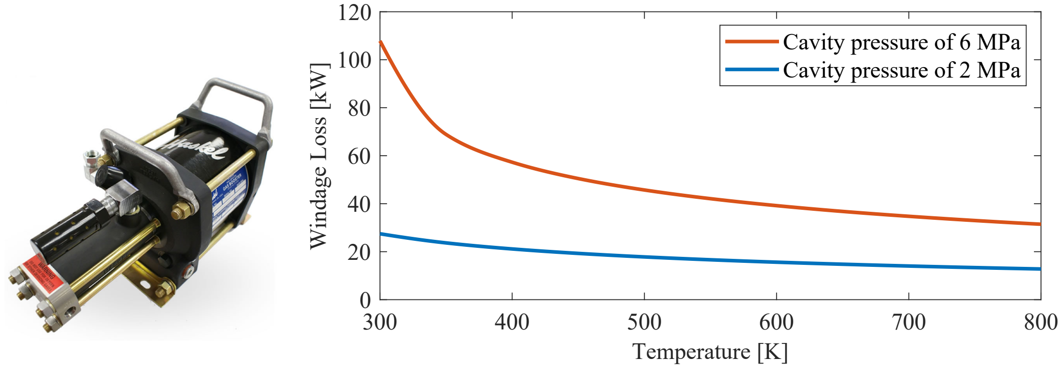

(a) (b)

Fig. 5: (a) Example scavenging pump [20], and (b) impact of pressure and temperature on windage loss.

3.1 Heat Sources in Motor Cavity

Typical heat sources in the motor cavity can be classified into four types: copper losses, iron losses, magnet losses, and windage losses. Copper losses arise from Joule heating in the stator windings. Iron losses occur in the laminated stator core as a result of alternating magnetic flux and comprise hysteresis losses and eddy-current losses, generated by circulating currents within the laminations. Magnet losses are primarily eddy-current losses induced in the permanent-magnets (PMs). Windage losses arise from viscous shear and turbulence of the working fluid; these losses scale strongly with rotational speed and become significant in high-speed hermetic environments.

To estimate these losses, a mixed analytical/FEA approach is adopted. Iron and magnet losses are evaluated using 2D FEA through commercial software JSOL JMAG, whereas copper and windage losses are computed analytically. Copper losses are obtained from the stator winding resistance and total conductor length, including end-winding effects [19].

Windage loss is the mechanical power dissipated by the fluid surrounding the rotor due to viscous drag from rotor and stator relative motion. While most literature on electric machine design studies consider atmospheric conditions (20 °C, 1 atm), where windage loss models are well established, this paper requires the use of an sCO_2 windage loss model, which is less known and involves more complicated physics. The Vrancik [21] model is utilized, where the following assumptions are made: (1) axial flow components are negligible; (2) the air gap thickness is small compared to both the rotor radius and its axial length; (3) the fluid is homogeneous, with no significant pressure gradient across the gap; and (4) the rotor is smooth, with no salient features. Under these assumptions, the total windage loss is expressed as:

$$P_{\mathrm{wr}} = \pi C_{\mathrm{d}}(\mathrm{Re})\,\rho\, r_{\mathrm{r}}^{4}\,\omega^{3}\,L_{\mathrm{r}} \tag{1}$$

where ρ is the fluid density, r_{r} is the rotor radius, ω is the angular speed, and L_{r} is the active rotor length. The Reynolds number (Re) and skin-friction coefficient (C_{d}) are determined as follows:

$$\mathrm{Re} = \frac{r_{\mathrm{r}}\,\delta\,\omega\,\rho}{\mu}, \tag{2}$$

$$\frac{1}{\sqrt{C_{\mathrm{d}}}} = 2.04 + 1.768\,\ln\!\left(\mathrm{Re}\sqrt{C_{\mathrm{d}}}\right), \tag{3}$$

Figure 5b shows the impact of pressure and temperature variations on the windage loss of the demonstrator machine introduced earlier. This calculation considers two cavity pressures, 2 and 6 MPa, where 2 MPa corresponds to the minimum and 6 MPa corresponds the maximum allowable pressures in the motor

Table 2: Specification parameters used in the optimization study [12].

Parameter	**Specification**
Rated speed	75 krpm
PM material	Recoma 26
Sleeve material	Carbon fiber
Stator lamination	Arnon5
Number of stator slots	24

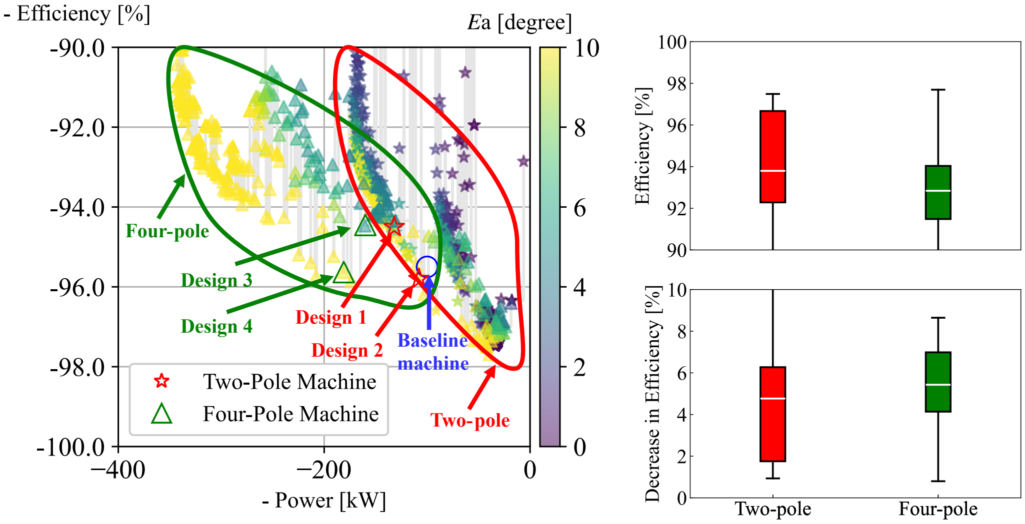

(a) (b)

Fig. 6: (a) Pareto fronts of two-pole and four-pole machines; efficiency and power calculated at rated speed and power with no unloading forces, while E_a is calculated during the unloading event, and (b) box and whisker plots for the efficiency decrease due to windage loss.

cavity [18]. As observed in Fig. 5b, higher pressure increases windage loss, primarily due to the corresponding increase in CO_2 fluid density. The increased windage loss raises heat generation in the motor cavity, which in turn elevates component temperatures. These trends underscore the need for effective thermal management to maintain lower cavity pressure and lower temperature within the allowable limits.

3.2 The Selected Machines

The authors in [12] conducted a multi-objective optimization for a surface PM machine (Fig. 4) using samarium–cobalt magnets (suitable for high temperatures) and ultra–thin-gauge stator lamination steel (to minimize core losses with high frequency). The original electric machine design from the hermetic turbomachine of Table 1 is included in Fig. 6a to serve as a baseline for comparing the optimization results in terms of power and efficiency. The winding layout was designed using the bridge winding configuration (see Fig. 3b) to act as a foil bearing unloader. The machine dimensions were optimized to maximize power and efficiency while minimizing torque ripple and force ripple. Power, efficiency, and torque ripple were evaluated at rated speed, while the force ripple was evaluated while unloading the shaft. The motor diameter and length were kept fixed to ensure that the optimized machines fit within the existing generator cavity of the existing turbomachinery system. Table 2 summarizes the specification parameters used in this optimization; for additional details regarding the optimization free variables or objective functions, the reader may refer to [12, Sec. IV].

Table 3: Performance parameters for four designs in the optimization study along with the baseline machine

Parameter	**Pole count**	**Power [kW]**	**Efficiency [%]**	**Torque ripple [%]**	E_a **[degree]**
Design 1	Two-pole	124	94.5	0.7	6.4
Design 2	Two-pole	109	95.8	0.3	15.8
Design 3	Four-pole	152	94.2	6.5	4.9
Design 4	Four-pole	181	95.7	14.6	49.6
Baseline machine	Two-pole	100	95.6	0.2	-

Figure 6a shows the resulting optimal Pareto fronts at the rated speed of 75 krpm for two-pole and four-pole electric machines with the bridge winding configuration. Although PM machines used in turbomachinery applications typically achieve efficiencies above 96% at full speed [22], the Pareto fronts indicate that achieving both high power and high efficiency simultaneously is not feasible in sCO_2 environment. For example, for the two-pole machines, no design with efficiency $> 96\%$ and power > 100 kW exists. The lack of these machines is due to sCO_2 environment rather than unloading forces since both power and efficiency are evaluated at rated speed and power, with no unloading forces.

To investigate this efficiency degradation, box and whisker plots of efficiency and the corresponding decrease in efficiency due to windage loss in the sCO_2 environment of the final Pareto front designs are illustrated in Fig. 6b. The decrease in efficiency is defined as

$$\text{Efficiency}_{\text{Atmospheric}} - \text{Efficiency}_{\text{sCO}_2},$$

As shown in Fig. 6b, four-pole machines experience a more pronounced efficiency reduction due to windage loss than two-pole machines. The median of decrease in efficiency for four-pole machines is approximately 6%, compared to approximately 3% for two-pole machines.

The Pareto fronts also reveal a clear trend between efficiency and the error if force vector angle E_a. Here, E_a is defined as the maximum angular deviation of the instantaneous force vector angle $\phi(\theta)$ from the desired value ϕ_avg over one mechanical revolution. The root cause of a non-zero E_a is space harmonics in the airgap magnetic fields due to the stator slotting, harmonic winding factors, or localized saturation. This metric is used to assess the smoothness of the unloading force. Designs with higher efficiency tend to exhibit larger error angles; for example, most of the high-efficiency designs ($> 96\%$) correspond to $E_a > 10°$. A large error angle indicates substantial force ripple on the foil surface, raising concerns about potential oscillatory loading on the foils, an effect that can be explored in future work.

To better illustrate the proposed unloader, this paper selects four machines for detailed analysis. The performance parameters of these designs are compared in Table 3. These machines are labeled in Fig. 6a as Design 1 and Design 2 for two-pole machines and Design 3 and Design 4 for four-pole machines. The following subsection discusses thermal considerations for electric machines in the sCO_2 environment, using Design 1 and Design 3 as examples of machines that balance machine power, efficiency, and error angle E_a.

3.3 Thermal Considerations

This subsection explains practical techniques for dissipating heat generated in the motor cavity and in the motor windings for the selected machines. As explained earlier, the selected machines from Fig. 6a are considered for use inside the motor cavity of the demonstrator of Fig. 4. The stator housing of this machine incorporates internal channels for water cooling and the machine is outfitted with two labyrinth seals that isolate the motor cavity from the sCO_2 flow. However, since the seals are not perfectly tight, leakage from both the turbine and compressor sides is inevitable. While this leakage can be a potential issue, it can also be utilized to cool the machine.

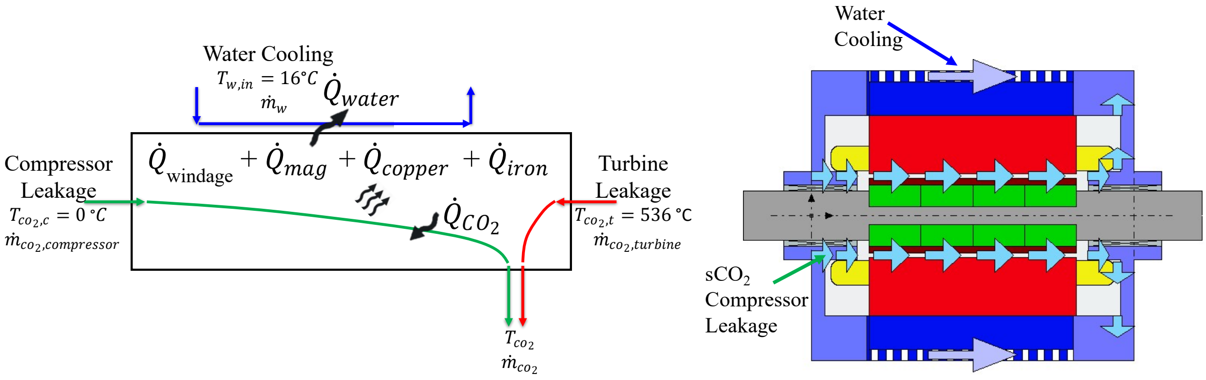

(a) (b)

Fig. 7: (a) Control volume of motor cavity, showing inputs, outputs, and water cooling feature, and (b) Ansys-MotorCAD model.

Typically, there are two leakage flows: one from the turbine side and one from the compressor side. The sCO$_2$ temperature on the turbine side is relatively high (approximately 550 °C), whereas the compressor-side leakage is comparatively cool and can be used to cool the motor cavity. This occurs due to the Joule–Thomson cooling effect, which results in a considerable temperature drop that can be exploited to cool the machine. The Joule–Thomson effect refers to the temperature change of a real gas when it expands through a flow restriction in an isenthalpic (throttling) process [23]. Therefore, to mitigate the impact of the hot turbine-side leakage and to take advantage of the cooler compressor-side leakage, the scavenging pump is connected to the turbine-side port, and the compressor-side port is plugged. This configuration draws the hot leakage directly out of the cavity while allowing the cooler leakage from the compressor side to sweep through the air gap and provide convective cooling.

The following assumptions are adopted to estimate the temperatures of the PMs and the stator windings: (i) the turbine-side leakage flow is completely scavenged, (ii) there is no pressure gradient across the air gap, and (iii) isenthalpic expansion occurs across the labyrinth seal. The first assumption means that only compressor-side leakage is present inside the motor cavity. The second assumption maintains the pressure inside the motor cavity at approximately 2 MPa using the scavenging pump to limit windage losses. The third assumption is used to estimate the inlet temperature of the compressor leakage due to the Joule–Thomson effect. This temperature drop is estimated from the pressure decrease between the upstream pressure of 17 MPa and the cavity pressure of 2 MPa, which results in a temperature reduction from approximately 65.6 °C to 0 °C. This temperature is considerably low, and the actual temperature will likely be higher due to windage heating occurring within the labyrinth seal; however, this approximation is considered reasonable at this analysis stage due to the isenthalpic assumption.

Figure 7a shows the simplified control volume of the motor cavity, indicating inlet and outlet flow rates along with the water-cooling features. This model will be used to obtain the temperature distribution in the motor cavity for the selected machines (Fig. 6a) using Ansys MotorCAD software (Fig. 7b).

4 Performance Analysis of the Selected Machines

This section presents the thermal analysis of the selected machines, as explained in Section 3.2, namely Design 1 and Design 3. First, it shows the distribution of machine losses within the motor cavity. Then, a demagnetization analysis is conducted to determine the maximum allowable temperature of PMs, followed by an analysis of the required sCO$_2$ compressor leakage flow rate and water-cooling flow rate needed to keep the motor within allowable temperature limits. Finally, it presents the performance of the generated

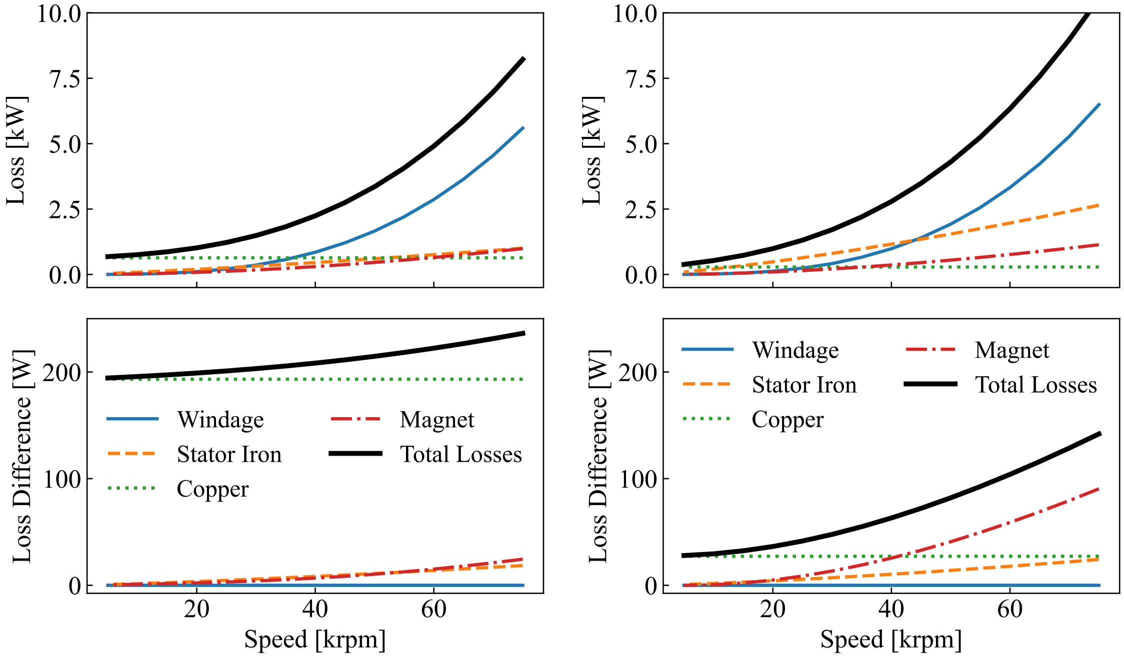

(a) (b)

Fig. 8: Machine losses and loss difference between motor and unloader for the selected (a) two-pole machine (Design 1), and (b) four-pole machine (Design 3).

suspension force during the unloading event.

4.1 Loss Analysis

The machine loss distribution of Design 1 and Design 3 over the operating speed range is shown in the top plots of Fig. 8 when the suspension force is disabled, i.e., the machine operates as a normal motor. For both machines, windage loss dominates at high speed, representing approximately 60% of the total losses at full speed, while stator iron and magnet losses increase more gradually. The four-pole machine exhibits noticeably higher losses than the two-pole machine (an increase of approximately 30%), mainly because the four-pole machine has a higher fundamental electrical frequency. The loss difference between the motor-only and the unloader modes is illustrated in the bottom plots of Fig. 8 and calculated as follows:

$$\mathrm{Loss}_{\mathrm{motor}} - \mathrm{Loss}_{\mathrm{Unloader}},$$

The results show no significant difference between the two operating modes. Interestingly, the unloader mode exhibits slightly lower losses; this occurs because the stator currents from both torque and suspension drives offset each other, resulting in a smaller net RMS current and, therefore, lower copper losses. Operating the selected two-pole machine (Design 1) to unload the shaft weight requires the use of 18% of the rated stator current for creating forces, leaving 82% available for producing torque, which results in an 18% reduction in output torque/power. This reduction only occurs while unloading forces are being created. At high speeds, when the unloading forces are turned off, the machine returns to its full torque/power rating. The behavior corresponds favorably to the torque requirements of turbomachinery driving centrifugal loads, where load torque increases with the square of rotational speed.

Since the machine losses heat the internal components, the safe operation of the motor is determined by their thermal limits, especially those of the stator windings and PMs. These components inherently define the

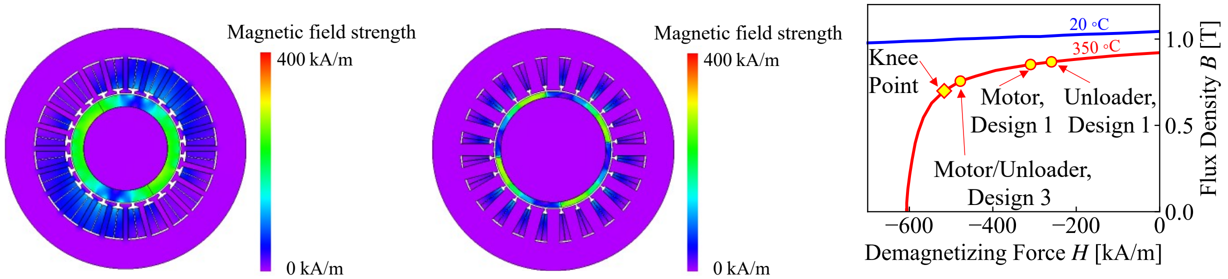

(a) (b) (c)

Fig. 9: Magnetic field distribution when the machine is operating as an unloader for the selected (a) two-pole machine (Design 1), and (b) four-pole machine (Design 3), and (c) the B–H curve for the PM at 20 °C and 350 °C, with the operating points for the selected machines [24].

maximum allowable operating temperature of the machine. The selected machines use NW-71 Class 220 for the winding coils, which have an allowable temperature of 220 °C. If the winding temperature exceeds the insulation class rating, the slot insulation can degrade, leading to short circuits and motor failure. The selected machines use samarium–cobalt magnets (Recoma 26). If the PMs overheat, demagnetization can occur. While the datasheet for Recoma 26 suggests operating the magnets at temperatures up to 350 °C [24] is feasible, electromagnetic analysis is required to ensure that no demagnetization occurs under the machine operating conditions.

4.2 PM Demagnetization Analysis

The allowable temperature of PMs depends on the machine operating points on the magnet B–H curve relative to the onset of irreversible demagnetization, referring to the knee point (Fig. 9c). Typically, demagnetization occurs when the demagnetizing force (external magnetic field) exceeds the knee point. From the Recoma 26 datasheet [24], the knee point can be defined at a demagnetizing force of approximately 500 kA/m. To determine the allowable temperature for the selected machines, two simulation studies are conducted: (i) torque production only (motor mode), and (ii) combined torque and force production (unloading event). Figure 9 shows contour plots of the magnetic field for the selected machines from the Pareto front (Fig. 6a). For Design 1, the maximum magnetic field strengths are 279 kA/m and 264 kA/m for the motor and the unloader, respectively. These operating points are plotted on the magnet B–H curve (Fig. 9c) and indicate that no demagnetization occurs at 350 °C. In addition, since the magnetic field strengths for both conditions are close, this indicates that no additional stress is created by the suspension field. Similarly, the magnetic field strength for Design 3 is 482 kA/m for both the motor and the unloader. However, this value is slightly lower than the allowable limit based on the knee point, suggesting that demagnetization may occur at 350 °C for Design 3. To avoid demagnetization, a 10% safety margin is adopted in this paper; that is, the allowable PM temperature is set to 315 °C.

4.3 Temperature Distribution for the Selected Machines

To calculate the temperatures of PM and winding for the selected machines using the loss distribution discussed in Section 4.1, the procedures and assumptions described in Section 3.3 are followed. Additionally, the compressor leakage and water-coolant flow rates are varied to determine the suitable combinations required to maintain PM and winding within their thermal limits, i.e., 315 °C for PM and 220 °C for the winding. Figure 10 presents the magnet and winding temperature distributions, along with the allowable temperature

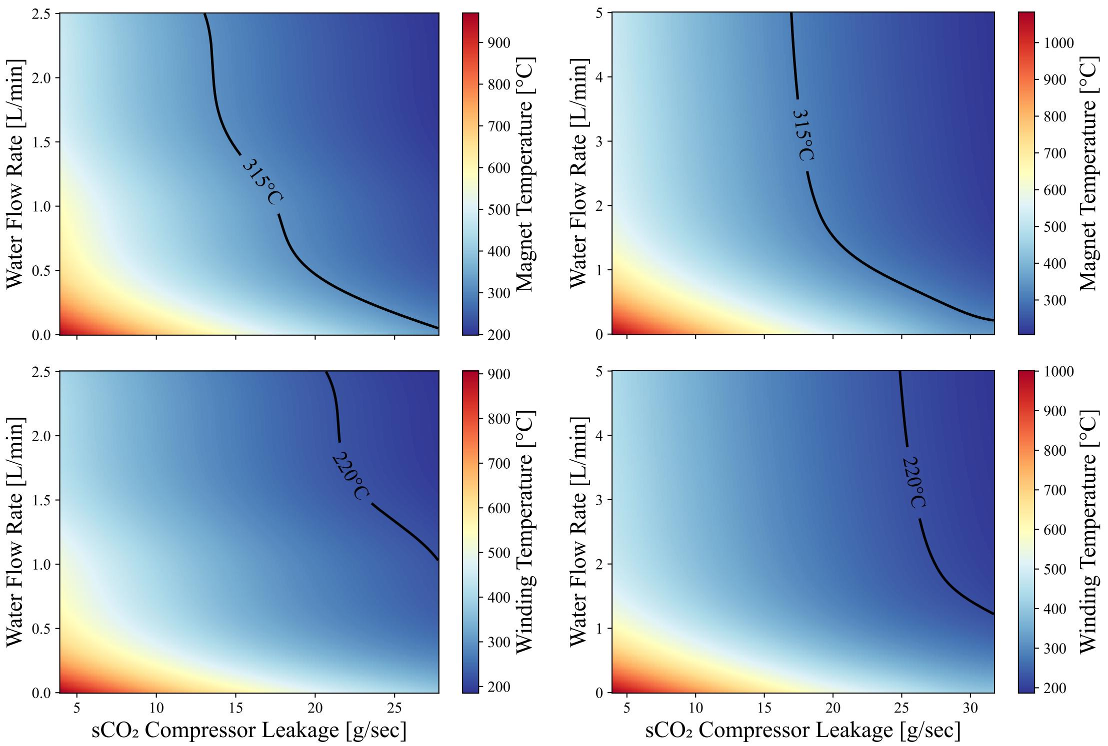

(a)

(b)

Fig. 10: Contour plots of magnet and winding temperatures for different combinations of sCO$_2$ compressor leakage flow and water coolant flow for (a) Design 1, and (b) Design 3.

contour lines.

For Design 1, safe operation of the PM (< 315 °C) is only achieved when the sCO$_2$ flow exceeds approximately 15 g/s and the water flow is greater than approximately 1.5 L/min. For the winding temperature, adequate cooling (< 220 °C) requires approximately 15–17 g/s of sCO$_2$ compressor leakage together with at least 1.5–2 L/min of water flow. When these conditions are not met, the winding temperature exceeds 800 °C due to insufficient convective heat removal.

As discussed in Section 4.1, the four-pole machine has higher electromagnetic losses, and therefore requires greater cooling capability. This trend is confirmed in Fig. 10b, which shows that Design 3 (the selected four-pole machine) requires increased water-cooling flow rates. For water flows of 3–5 L/min, the winding temperature remains below 220 °C when the sCO$_2$ flow exceeds 20 g/s. Although the magnets are less directly influenced by water flow than the windings, increasing the water-cooling rate still provides benefit. For water flows above 3 L/min, the magnet temperature remains below 315 °C when the sCO$_2$ compressor leakage is approximately 18 g/s.

For both machines, leakage flow on the order of 20 g/s is sufficient to keep PM and winding temperatures within their allowable thermal limits. In practice, reducing the compressor leakage is preferred to minimize scavenging-pump power. However, selecting an optimal flow rate that both cools the motor and reduces pumping power is challenging, since leakage flow depends on the labyrinth-seal design and the compressor upstream pressure [18]. For the selected machines, a leakage flow of 30 g/s is chosen as a target value to reduce scavenging-pump power while remaining consistent with the thermal study requirements.

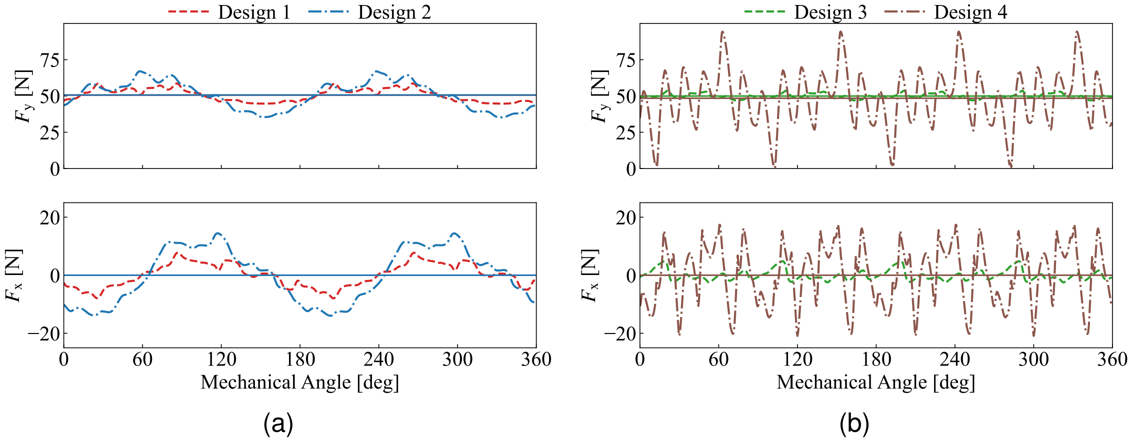

(a)

(b)

Fig. 11: Force performance during unloading event at speed of 5 krpm for four designs (a) two-pole machines, and (b) four-pole machines.

4.4 Machine Force Performance During Unloading

As discussed in Section 3.2, the Pareto front (Fig. 6a) shows a trade-off between maximizing efficiency and reducing force error angle (E_a). To investigate machines with higher efficiency but larger E_a, all four designs discussed earlier in Section 3.2 are now investigated to examine their force ripple.

Figure 11 compares the force performance of these four designs at 5 krpm, where the force is produced only in y-axis (referred to as F_y) to illustrate the unloading event, while the force along the x-axis F_x should ideally be zero. Figure 11a shows the analysis results of F_y and F_x in the two-pole machines, where Design 1 exhibits a relatively smooth F_y waveform, achieving the required average radial force with minimal disturbance in F_x. Design 2, which has an efficiency of approximately 95.8% and a larger error angle (15.8°), results in higher force ripple in both directions compared to Design 1. Figure 11b shows the analysis results of F_y and F_x in the four-pole machines, where Design 3 shows similarly smooth force behavior, maintaining the desired average F_y with low ripple. In contrast, Design 4 shows a higher error angle (49.6°), although offering higher efficiency of 95.7% and higher output power of 181 kW. This large angular deviation leads to high oscillations in both F_y and F_x,

5 Conclusion

This paper investigated the practical implementation of electric machines acting as foil bearing unloaders in the sCO$_2$ environment. The paper first presents the design space of electric machines capable of acting as foil bearing unloaders for an existing hermetic sCO$_2$ turbomachine with a lower pressure generator cavity. It is found that the electric machine of this existing turbomachine design can be “upgraded" (with the same overall length and diameter) to act as a foil bearing unloader while retaining its nameplate power (100 kW) and efficiency (95.6%) ratings. For this turbomachine, the paper shows that exceeding the combined ratings of 100 kW and 96% efficiency is not feasible due to the high windage loss of the sCO$_2$ environment for two pole electric machines. Four pole electric machines are shown to have potential to reach higher power ratings, but the highest efficiency designs suffer from poor unloading force performance. This is likely not an inherent limitation of the unloader concept, as the authors believe it can be solved by utilizing a different number of stator slots.

The paper considered the thermal management of the proposed foil bearing unloading machines and finds that these machines do not impose any additional thermal constraints. The paper discussed techniques unique to the sCO_2 environment to keep electric machine components within their allowable temperature limits. The paper showed how a scavenging pump can be utilized to draw compressor leakage through the motor air gap to cool the machine. FEA was employed to determine the heat loading and thermal resistance networks were used to estimate the temperature distribution in the motor cavity. The unloading mode of operation (occurs at low speed and torque) was found to correspond to reduced demagnetization risk and lower rotor heat generation. The most significant thermal loads occur during standard motor operation at rated power and maximum speed, when the foil bearings do not require unloading forces. The results indicate that to keep the PMs and windings within thermal limits, combinations of sCO_2 compressor leakage (> 20 g/s) and water-coolant flow (> 2 L/min) are required.

In conclusion, this paper shows that the proposed electric machines can practically generate foil bearing unloading forces in hermetic sCO_2 environments without compromising the electric machine's nameplate ratings (efficiency and power) since the unloading forces do not result in additional thermal load, are only required during start up / shutdown, and the force producing currents can be fully redirected to torque production when no unloading forces are required.

Acknowledgements

Sandia National Laboratories is a multimission laboratory managed and operated by National Technology & Engineering Solutions of Sandia, LLC, a wholly owned subsidiary of Honeywell International Inc., for the U.S. Department of Energy's National Nuclear Security Administration under contract DE-NA0003525.

This paper describes objective technical results and analysis. Any subjective views or opinions that might be expressed in the paper do not necessarily represent the views of the U.S. Department of Energy or the United States Government.

FEA tools used in this work were provided by the JSOL Corporation (JMAG).

The thermal simulations used in this work were conducted using ANSYS Motor-CAD (Release 2025 R2, ANSYS).

References

[1] M. T. White, G. Bianchi, L. Chai, S. A. Tassou, and A. I. Sayma, “Review of supercritical CO2 technologies and systems for power generation,” *Applied Thermal Engineering*, vol. 185, p. 116447, 2021.

[2] Y. Ahn, S. J. Bae, M. Kim, S. K. Cho, S. Baik, J. I. Lee, and J. E. Cha, “Review of supercritical CO2 power cycle technology and current status of research and development,” *Nuclear engineering and technology*, vol. 47, no. 6, pp. 647–661, 2015.

[3] T. Noguchi, W. Chan, N. Petersen, L. Rapp, and E. Severson, “Opportunities to Enhance sCO2 Power Cycle Turbomachinery with Bearingless Motor/Generators,” *Solar Compass*, vol. 12, p. 100094, 2024.

[4] J. Vaidya and E. Gregory, “High speed induction generator for applications in aircraft power systems,” *SAE transactions*, pp. 1830–1836, 2004.

[5] E. Tkacz, Z. Kozanecki, and J. Łagodziński, “High-speed hermetic turbogenerator with a hybrid bearing system,” *Journal of vibration engineering & technologies*, vol. 6, pp. 325–331, 2018.

[6] C. DellaCorte, “Oil-free shaft support system rotordynamics: Past, present and future challenges and opportunities,” *Mechanical Systems and Signal Processing*, vol. 29, pp. 67–76, 2012.

[7] B. Ertas, “Enabling bearing technologies for high-power oil-free turbomachinery,” in *Proceedings of the American Society for Precision Engineering (ASPE) 2019 Annual Meeting*, (Nashville, TN, USA), American Society for Precision Engineering, 2019.

[8] T. C. Allison, J. C. Wilkes, J. J. Moore, and K. Brun, “Turbomachinery Overview for Supercritical CO2 Power Cycles,” tech. rep., Turbomachinery Laboratory, Texas A&M Engineering Experiment Station, 2017.

[9] J. L. Preuss, “Application of hydrostatic bearings in supercritical CO2 turbomachinery,” *The 5th International Supercritical CO*, vol. 2, 2016.

[10] S. Priyadarshini and S. K. Behera, “A comprehensive review on advancements in compliant structures of gas foil journal bearings,” *Proceedings of the Institution of Mechanical Engineers, Part J: Journal of Engineering Tribology*, vol. 238, no. 9, pp. 1039–1065, 2024.

[11] C. DellaCorte, V. Lukaszewicz, M. J. Valco, K. Radil, and H. Heshmat, “Performance and durability of high temperature foil air bearings for oil-free turbomachinery,” *Tribology transactions*, vol. 43, no. 4, pp. 774–780, 2000.

[12] S. Saleh, T. Noguchi, L. Rapp, and E. Severson, “Design of bearingless motors to unload static forces from foil bearings,” in *Proceedings of the IEEE Energy Conversion Congress and Exposition (ECCE)*, 2025.

[13] P. Rao, P. Sheaffer, Y. Chen, U. Karki, and P. Fitzgerald, “Us industrial and commercial motor system market assessment report volume 3: Energy saving opportunity,” 2022.

[14] E. Swanson, H. Heshmat, and J. Walton, “Performance of a foil-magnetic hybrid bearing,” *J. Eng. Gas Turbines Power*, vol. 124, no. 2, pp. 375–382, 2002.

[15] J. Chen, J. Zhu, and E. L. Severson, “Review of bearingless motor technology for significant power applications,” *IEEE Transactions on Industry Applications*, vol. 56, no. 2, pp. 1377–1388, 2019.

[16] A. O. Salazar, A. Chiba, and T. Fukao, “A review of developments in bearingless motors,” in *Proc. 7th Int. Symp. Magnetic Bearings*, pp. 335–340, 2000.

[17] A. Khamitov, N. P. Petersen, and E. L. Severson, “Combined windings for bearingless motors—an overview,” in *2023 IEEE Energy Conversion Congress and Exposition (ECCE)*, pp. 4628–4635, IEEE, 2023.

[18] S. A. Wright, R. F. Radel, M. E. Vernon, P. S. Pickard, and G. E. Rochau, “Operation and analysis of a supercritical CO2 Brayton Cycle,” tech. rep., Sandia National Laboratories (SNL), Albuquerque, NM, and Livermore, CA, 2010.

[19] N. Bianchi, S. Bolognani, and P. Frare, “Design criteria for high-efficiency spm synchronous motors,” *IEEE Transactions on Energy Conversion*, vol. 21, no. 2, pp. 396–404, 2006.

[20] Nuvair, “Haskel single stage, single acting booster.” `https://nuvair.com/ag-7.html/`, 2025. Accessed: 2025-10-29.

[21] J. E. Vrancik, “Prediction of windage power loss in alternators,” NASA Technical Note D-4849, NASA Lewis Research Center, Cleveland, OH, October 1968.

[22] D. Gerada, A. Mebarki, N. L. Brown, C. Gerada, A. Cavagnino, and A. Boglietti, “High-speed electrical machines: Technologies, trends, and developments,” *IEEE transactions on industrial electronics*, vol. 61, no. 6, pp. 2946–2959, 2013.

[23] O. Kon and İ. Caner, “Investigation Of Heat Transfer and Joule-Thomson Effect in Wells of Depleted Oil and Gas Reservoirs Used For Carbon Dioxide (CO2) Storage,” *El-Cezeri*, vol. 12, no. 3, pp. 298–310, 2025.

[24] A. M. Technologies, “Recoma® smco grades.” `https://www.arnoldmagnetics.com/wp-content/uploads/2017/10/Recoma-Combined-160301.pdf`, 2017. Accessed: Nov. 2025.